Rock uplift rates revealed by Earth's largest volcanic eruptions

Authors: B. A. Adams*[1] F. J. Cooper[1], C. Walsh[1], and K. V. Cashman[1,2]

Affiliations:

[1]School of Earth Sciences, University of Bristol, Bristol, UK

[2]Department of Earth Sciences, University of Oregon, Eugene, Oregon, USA

*Correspondence to: Byron.Adams@bristol.ac.uk

Abstract: Pyroclastic density currents associated with large explosive volcanic eruptions can generate expansive ignimbrite deposits characterized by planar, low-angle surfaces. Here, we demonstrate the utility of these planar surfaces for constraining pre-eruptive rock uplift rates based on the relief of buried paleolandscapes. Using a landscape evolution model that focuses on the process of river incision, we explore the range of permissible landscape geometries beneath an ignimbrite of given surface slope. We demonstrate an excellent relationship between river channel relief and range-scale slope as a function of rock uplift rate. We show that rock uplift rates, which generate range-scale slopes lower than that of the overlying ignimbrite surfaces, are reliable solutions for long-term rates. We focus our study on the Miocene ignimbrites of the Oxaya Formation on the western flank of the Andes, where we estimate pre-eruptive rock uplift rates of < 0.25 km My^{-1}, comparable with independent constraints from thermochronologic and geothermobarometric studies.

INTRODUCTION

Subduction zones at convergent plate margins are home to some of Earth's largest mountain ranges and most of its explosive volcanoes. A prime example is the Central Andes in South America, where continuous subduction since the early Jurassic (*1*) has generated >2.5 km of relief and some of the largest-known ignimbrite-forming eruptions (*2, 3*). The persistence of these high-elevation regions over geologic time makes them important places to examine the long-term growth of mountain ranges (*4, 5*), the role that volcanism has played in shaping them (*2*), their influence on climate at both a regional and global scale (*6–8*), as well as the evolution of regional biospheres (*9*).

Better understanding the evolution of mountain ranges and the external changes they affect, requires knowledge of the history of the deformation of the rocks that form them, specifically the velocity of rocks as they move away from a fixed datum, like the Earth's center, or rock uplift rate. However, quantifying rock uplift rates is fraught with challenges as it is notoriously difficult to determine. One option is to constrain the history of surface uplift, which occurs when the rock uplift rate is greater than the erosion rate (which acts to remove material from the surface). Surface uplift rates can be measured directly via changes in altitude found in stable isotopic compositions of precipitates or biota (*6*). Most constraints on erosion rely on geochemical proxies such as thermochronometric cooling histories (*10*) or geobarometric and geochronologic constraints (*11, 12*).

Because these techniques are only proxies for rock uplift rates, each requires a numerical model to convert primary observations (e.g., cooling ages, stable isotope concentrations, or pressures) into velocities. While these models are essential, they introduce a level of uncertainty associated with other unconstrained variables within each model. In

addition, the temporal resolution of a geochemical proxy is limited by the underpinning dates it is associated with. For example, an erosion history from a single thermochronometric system could have a high temporal resolution over a short time interval (from the cooling age to the present) for a young sample, or a low resolution over a longer time interval for an older sample.

An alternative approach derives the long-term rock uplift rate from the topographic relief that it has created, on the basis that relief is heavily influenced by and proportional to rock uplift rate (*13*, *14*). In studies that use landscape evolution models to invert topography, there is a characteristic timescale of landscape response and adjustment (*15*) that provides an estimate of the temporal resolution of the rock uplift rate solution. Building on this approach, we describe a new method for constraining rock uplift rates in tectonically-active volcanic regions such as the Central Andes where landscapes have been buried by large-volume, spatially expansive ignimbrites (*2*). We demonstrate how the planar, low surface slopes characteristic of these volcanic deposits can be used to estimate the relief of the buried paleolandscape, and thus the pre-eruptive rock uplift rate.

Starting with the assumption that most mountain range relief is set by the geometry of river channel networks, we drive a landscape evolution model with a form of the stream-power model for river incision to demonstrate how rock uplift rates fundamentally control the perpendicular range-scale slope, which is the first-order requirement for burying a landscape with a fluidized deposit (Fig.1). We capitalize on the relationship between river incision and relief, range-scale slope, and rock uplift rates to constrain rock uplift rates of < 0.25 km My^{-1} on the western flank of the Central Andes for a period of ~14 Myr prior to a major ignimbrite flare up in the early Miocene (~22 Ma). These rates are consistent with long-term rock uplift rates derived from low-temperature thermochronometry studies in the region, e.g. <0.2 km My^{-1} since ~50 Ma (Avdievitch et al. 2018) and 0.25 km My^{-1} since ~80 Ma (Stalder et al., 2020). They can also be compared directly with rates over a similar pre-eruption time window derived from geothermobarometric constraints on pre-ignimbrite exhumation, ~0.33 km My^{-1} from ~22 – 40 Ma (*12*). This Andean example is an illustrative case study of the potential to use volcanic deposits to constrain rock uplift rates in other areas with a history of explosive volcanism, such as the Cordilleras of Northern, Central and South America, and New Zealand, providing a new tool to constrain rock uplift histories around the world.

VOLCANISM ON THE WESTERN ANDEAN MARGIN

The western margin of the Central Andes in northern Chile and southern Peru is defined by a magmatic arc that has evolved in response to continuous subduction of the Farallon plate beneath South America since the early Jurassic (*1*). Over time, explosive volcanism has blanketed much of the region, most notably by the large-volume ($>1,260$ km^3; *16*) early Miocene Cardones ignimbrite at 21.9 Ma (*2*).

The Cardones forms part of the Oxaya Formation, a series of four gently west-dipping ignimbrites thought to have been deposited during volcanic flare-up related to accelerated plate convergence rates as the subducting slab steepened and flat slab subduction ended (*17*). Zircon crystallization ages constrain the flare-up in northern Chile to a 3 Myr period, starting at ~23 Ma (*2*). Although the Cardones ignimbrite has experienced significant deformation since its deposition, van Zalinge and others (*2*) performed a line-balanced reconstruction to determine that it had an initial surface slope of $1.5 \pm 0.3°$, and paleomagnetic analysis of fabrics within the ignimbrite established a local transportation direction of 247°, deriving from the nearby Lauca Caldera (*3*).

Dynamics of ignimbrite deposition

Ignimbrites are matrix-supported, pumice-dominated deposits left behind by pyroclastic flows (*18*). While smaller ignimbrites are generally created by dome collapse (*19*),

larger volume deposits are created by pyroclastic density currents triggered by the collapse of Plinian eruption columns or large-scale calderas (*20*). Some of the largest ignimbrite deposits may have been formed from complex calderas typical of volcano-tectonic depressions (*21*). Small volume eruptions (~1–10 km^3) typically produce valley-confined ignimbrites, but the largest caldera-forming eruptions (100 - > 1000 km^3) can create regionally extensive deposits, which may have had a preferential flow direction, form large areas of new smooth topography with a very low slope and are referred to as low aspect ratio ignimbrites (LARIs) (*22*) (Fig. 1). A key attribute of these deposits is that the deposit is thicker over the paleo-valleys than over the paleo-ridges (*25*). Very large ignimbrites (M > 8 using the scale of Mason et al. 2004) can travel distances well over 100 km from their source and can exceed 1 km in thickness, demonstrating that these deposits record some of the most destructive eruptions in Earth's history.

The modern morphology of a LARI surface is the result of the initial deposit surface, lithospheric deformation, and the subsequent erosion or deposition of materials as other surface processes, such as river incision or hillslope transport, are re-established. The initial morphology of the ignimbrite surface can be affected by many factors including: the discharge rate of the eruption, the pre-existing surface topography, and the fluidized state of the flow (*23*). Many LARI deposits form relatively flat, expansive surfaces with a gentle dip (0.5°–3°) away from the source vent (*2*).

There are three simple relationships that are possible between the ignimbrite surface and the topography that it has overridden (Fig 1). 1) The ignimbrite surface could be steeper than the range-scale slope of the buried landscape. This is in-line with the observation that ignimbrite deposits generally thin away from the source. 2) The ignimbrite surface could be less steep than the buried surface. This is not a condition that we would consider to be likely over large distances with thick deposits, as this would require ignimbrites to thicken considerably away from the source, which is not a common observation/mode of deposition. 3) The ignimbrite surface slope could be roughly equal to the range-scale slope of the underlying landscapes. From this we conclude that the baseline condition for covering a landscape with an ignimbrite is that the range-scale slope of the maximum elevations of the paleo-topography must be equal to or less than the slope of the initial ignimbrite surface.

CONTROLS ON CONTRACTIONAL OROGEN RELIEF

Flat, LARI deposits make excellent datums because of their expansive nature and the ability to date them using radiometric techniques. These paleo-markers have been used for constraining rock deformation (*2*); our aim is to use the slope of an ignimbrite surface to constrain both the pre-eruption topography and the conditions that formed that paleo-topography. Given the plausible juxtaposition of range-scale slopes and slopes of overlying volcanoclastic deposits, we seek a method of generating physically possible landscapes that can be compared with observations from natural volcanic landscapes. We test possible landscape geometries by generating hundreds of synthetic terrains with a wide array of boundary conditions. We stream-line our modelling efforts by developing a landscape evolution model that captures the evolution of river networks, which make up at least 80% of the relief of most mountain ranges (*24*). This simple workflow allows us to test ideas about the influence of rock uplift rates without being over-parametrized and under-constrained.

The stream-power model

To assess the influence of rock uplift rate on the relationship between fluvial relief and range-scale slopes, we start with the conservation of mass and the classical stream-power model of river incision (*15, 25*):

$$\frac{dz}{dt} = U(x,t) - E(x,t) \tag{1}$$

$$E(x,t) = K(x,t) \, A(x,t)^m \, S(x,t)^n \tag{2}$$

where $\frac{dz}{dt}$ is the surface uplift rate (z is the elevation of a river bed in meters, t is time in years, and x is river distance in meters), U is the rock uplift rate (m yr^{-1}), E is the erosion rate (m yr^{-1}), K (units depend on m, when $m = 1$, the units are m^{-1} yr^{-1}) is the coefficient of erosion, often referred to as erosional efficiency or erodibility, which encapsulates the influence of environmental conditions such as climate, lithology, and incision process (e.g., abrasion, plucking, etc.), A is the drainage area (m^2), S is the channel slope (dimensionless), and m and n are dimensionless exponents related to runoff variability, channel incision processes, and hydraulic geometry.

In quasi-steady-state landscapes, here defined as landscapes where erosion and rock uplift are roughly balanced and topography is invariant over time (i.e., $U = E$ and $\frac{dz}{dt} = 0$), stream power model predictions agree with the observation that local channel slopes are inversely proportional to drainage area (26, 27) and, in natural landscapes, erosion rates scale as a power function of channel slope and drainage area (25). As a result, quasi-steady-state river channels produced by the stream-power model, and those found in nature, have concave-up forms that make it difficult to discern meaningful changes in local channel slope. To counteract this affect, local channel slopes can be adjusted for the downstream increase in drainage area using the relationship

$$S(x) = k_s \, A(x)^\theta, \tag{3}$$

where θ is a dimensionless constant that measures the concavity of a longitudinal river profile and the coefficient, k_s, is the measurement of channel steepness (22, 23). Channel steepness allows comparison of the relief of river channels regardless of the magnitude of the areas they drain. Channel steepness can be calculated from topographic data where local channel slopes can be measured and concavity (θ) can be estimated from regressions of S and A (25). Alternatively, channel steepness can be measured by regressions of a chi-plot, a channel profile where river distance is replaced by a new distance term χ (m) that accounts for the change in drainage area and concavity

$$k_s = \frac{z(x)}{\chi(x)} \tag{4}$$

$$\chi(x) = \int_0^x \left(\frac{A_0}{A(x)} \right)^\theta dx, \tag{5}$$

where A_0 is a reference area used to simplify the units of the integral. Here we use a reference area of 1 m^2 for simplicity. To compare channel steepness values from different landscapes it is necessary to use a single θ value, referred to as θ_{ref}. When θ_{ref} is implemented in a suite of landscapes, the term normalized channel steepness (k_{sn}) is used. In this paper, all channel steepness values are calculated with θ_{ref}, however, for simplicity we will use the term channel steepness. Channel steepness is a robust geometric measure for understanding the importance of spatial changes in channel relief that can be measured without any knowledge of climate, rock type, or river incision process. In quasi-steady-state landscapes with spatially uniform lithology, climate, and rock uplift conditions, landscapes tend to have a single channel steepness value and the concavity is equal to the ratio of m and n from the stream-power model (i.e., $\theta = m/n$) (19).

To link the relief of river channels to rock uplift rates, we combine equations 1, 2, and 3, assuming quasi-equilibrium conditions, to find:

$$k_{sn} = K^{-1/n} \, E^{1/n} \tag{6a}$$

$$k_{sn} = K^{-1/n} \, U^{1/n}. \tag{6b}$$

Equation 6b shows that channel steepness is proportional to rock uplift rate and inversely proportional to erodibility.

Erodibility of river channel rocks

Measuring the erodibility of river channel rocks is not straightforward because an accurate history of recent erosion is often required. The most common method for estimating erodibility calculates local river incision rates within systems by comparing the form of the present and a paleo-channel of known age using the stream-power model (eq. 1 and 2). From these rates and the measured values of S and A, values of m, n, and K can be estimated by minimizing the misfit between observed and modelled channel profiles (*28–30*). Erodibility has been shown to vary over several orders of magnitude for different rivers even when m and n are held constant (*28*). More recent methods that isolate the effects of rock type alone suggest, however, that the erodibility of relatively competent and softer rocks may vary by only an order of magnitude (*31, 32*). Where the influences of rainfall on erodibility in natural landscapes are included, it appears that higher rainfall rates increase erodibility (*14, 31, 33*). Of these studies, the most significant impact of rainfall has been suggested in the Himalaya where erodibility may scale proportionally with mean annual rainfall, and high rainfall rates can subdue topographic relief and mask high rock uplift rates (*14*).

Non-linearity of the stream-power model

Equation 6 shows the power-law dependency of erosion rates on river channel relief. In theory, in quasi-steady-state landscapes the ratio of m/n is equal to the concavity of river channel profiles, so that there should be some combination of n, m, and K values that fits the relationship of E or U and channel steepness. Concavity values do vary in natural systems but generally lie between 0.35 to 0.65, with most values close to 0.5 (*34*). While values of m and n have been estimated from inverting river channel profile data (*28*), n values that result from these analyses are highly variable even though a consistent regional value might be expected. To investigate the problem from a more regional perspective, researchers have used relationships between channel steepness and basin-average erosion rates derived from cosmogenic nuclides (i.e., equation 6a) to constrain n (*35, 36*). Regressions of erosion rates and channel steepness also estimate n to vary, generally from 1 to 2 (*37, 38*).

RESULTS
Relative influence of erodibility and rock uplift rate on range-scale slopes

If rivers had perfectly linear plan-view channel geometries (here referred to as the channel topology) and flowed perfectly perpendicular to a mountain range, equations 4, 5, and 6b could be used to calculate the slope of the range. However, because river networks have complex topology such that river distance is greater than the range-perpendicular distance, the range-scale slope must be calculated numerically within a 2D model. We built our model starting with the framework provided by Landlab (*39*), an open-source, Python-based toolkit that provides a platform for understanding the processes that act on planetary surfaces. The results of our experiments are illustrative of the first order control of rock uplift on topographic slope and the trade-off between rock uplift rate and bedrock erodibility. We do not seek a best-fit outcome to constrain a full suite of model parameters to explain any specific topography. Instead, we focus only on synthesizing landscapes that help us quantify relationships between range-scale relief, fluvial relief, and rock uplift rate.

Initial experiments were performed on a 22.4 × 22.4 km (~500 km^2) regular grid of 200 m node spacing with a southern open boundary. To reduce the time to steady-state, and thus processing time, we initialized each model with an elevation dataset that included an existing river channel network with a total relief of 10 m. For each experiment we assumed a spatially and temporally uniform rock uplift rate and erodibility (see GitHub link for full codes in Jupyter Notebooks). We allowed the landscape to evolve until a steady-state topography was reached whereby channel steepness values and erosion rates became stable over space and time and erosion rates were equal to the imposed rock uplift rate.

Within our experiments, we varied rock uplift rates from 0.1 to 2 km Myr^{-1} and erodibility from 1 x 10^{-9} to 1 x 10^{-6} m^{-1} yr^{-1} to produce 560 synthetic landscapes. We also tested different initial channel topologies but found this did not change the resulting topographic metrics or our conclusions. We use $n = 2$ and $m = 1$ for all model runs as values of $n > 1$ appear most appropriate in many tectonically active settings (*14, 37, 38, 40*). First-order results do not rely on choices of m or n provided the ratio between the two is maintained and comparable to natural landscapes although, in detail, the non-linear dependence of erosion rate on slope (i.e., $n = 2$) will affect the fluvial relief for a given K value. In other words, using $n = 2$ requires smaller values of K (compared to $n = 1$) to produce natural topographies at the same rock uplift rate (Fig S1). This demonstrates the stream-power model requirement to have balanced n, m, and K values when comparing synthetic and natural landscapes. From the resulting steady-state topography of each K and U combination, we calculate the mean channel steepness and the range-perpendicular slope of the maximum elevations, which we refer to as the range-scale slope (S_R). We calculate the channel steepness using equation 4 and the range-scale slope by regressing (least-squares fit) the maximum elevations of the swath profile of the entire landscape (e.g., Fig. 2). Because we use the chi method (eq. 4) and a concavity value of 0.5 for calculating channel steepness, our resulting values are unitless. For a given erodibility, rock uplift rate is proportional to the range-scale slope and channel steepness (Fig. 2). Because n is greater than 1, linear changes in rock uplift rate induce non-linear changes in topographic relief.

Range-scale slope is linearly related to channel steepness (Fig. 3a) because the slope of the relationship is sensitive only to the ratio of our fixed m and n values. Figure 3b shows the contours of channel steepness and range-scale slope from our model results through the solution field. The relationship between channel steepness and range-scale slope (Fig. 3a) allows us to calculate an analytical solution for a range-scale slope given a U and K pair defined by equation 6 (thin lines in Fig. 3b). At lower rock uplift rates and lower erodibility values, both sets of contours converge toward a rock uplift rate of 0 km Myr^{-1}. Higher rock uplift rates cause the contours to become roughly parallel; higher erodibility values increase the distance between the contours.

To bury a paleo-landscape with an ignimbrite we require that the initial deposit surface has a slope equal to or greater than that of the buried topography. Therefore, for our Andes example, we are most interested in exploring the suite of landscapes whose range-scale slope is ≤ 1.5°. This low-slope topography restricts parameter space (only parameter space above the 1.5° contour in Fig. 3b is permissible), but not enough to narrow the range of possible rock uplift rates.

Constraints from existing estimates of erodibility

In addition to constraining parameter space based on observations of ignimbrite slopes, we can further constrain parameter space within our synthetic landscape dataset by using existing estimates of erodibility in natural landscapes. As part of this analysis, we used the technique of Barnhart et al., (*41*) to convert published erodibility values calculated by varying m and n to values comparable to those used here, where $m = 1$ and $n = 2$ (see Table S1). All values discussed here have been recalculated. Stock and Montgomery (*28*) produced estimates of erodibility from around the globe. Here we have re-analyzed their data from four rivers which traverse granites and metasedimentary rocks in south-eastern Australia yielding values from 2 x 10^{-9} to 2 x 10^{-8} m^{-1} yr^{-1} and four rivers which flow over basalts in Kauai (USA) yielding values from 3 x 10^{-9} to 5 x 10^{-9} m^{-1} yr^{-1}. When van der Beek and Bishop (*30*) reexplored Stock and Montgomery's Australian field area they calculated erodibility values of ~2 x 10^{-9} m^{-1} yr^{-1}. A wide range of erodibility values, ~ 2 x 10^{-9} to 1 x 10^{-8} m^{-1} yr^{-1}, have been calculated for Himalayan igneous and sedimentary derived metamorphic rocks, although this range may reflect spatially variable rainfall and not rock properties (*14*). Using the equations of Adams et

al. (*14*) and the suggestion of arid conditions in the Miocene Andes (*42*), an erodibility value would likely be ~ 1 x 10^{-9} m^{-1} yr^{-1}.

More locally, the presence of the Miocene ignimbrites themselves provide useful insight into plausible values of erodibility. Given that the river network has struggled to remove the ignimbrite deposits in ~20 Myr, and there are knickpoints that are at least 11 Myr old in the western Andes (*43, 44*), timescales of response are long, and therefore, erodibility values are low (i.e., Fig. 3c), the likely effect of an arid environment. Indeed, Fox et al. (*45*) invert modern topography to suggest a value of 8 x 10^{-9} m^{-1} yr^{-1} for the western flank of the Peruvian Andes.

If we take a conservative one order of magnitude estimate of plausible erodibility values (1 x 10^{-9} to 1 x 10^{-8} m^{-1} yr^{-1}), rock uplift rates are constrained to < 0.25 km Myr^{-1} for topographies with slopes ≤ 1.5° (Fig. 3b). This suggests that the landscapes buried by the ignimbrites on the western Andean slope in northern Chile were of relatively low relief before the Miocene flare-up (k_{sn} < 160) due to the relatively low rock uplift rate.

Constraining time scales of landscape response

Because the times scale of landscape response is a function of river length or drainage area, we performed a smaller suite of model runs (60) on larger spatial scales (100 x 50 km) to estimate time scales of response closer to what we might expect from the Miocene Andes. For these simulations we used analytical solutions for erodibility values (Fig. 3b) and the same range of rock uplift rates as above and range-scale slope values of 0.5°, 1.0°, and 1.5°. These models were also initiated with a topography that has a developed river network and a maximum relief of 10 m. As the adjustment between two steady-states follows an exponential temporal path in our models, we report the time scale of response at the 95% level, instead of the 100% level, which can be considerably longer despite the insignificant difference in topography (*46*). Figure 3c demonstrates the effect of rock uplift rate, erodibility, and final topographic relief on the timescale of response. The landscapes with the lowest erodibility and rock uplift rate, and highest final relief, take the longest to achieve a new steady state.

DISCUSSION
How well can the stream-power model describe buried landscapes?

While the stream-power model might appear overly simplistic for the complex problems of river incision and defining the geometry of unobservable landscapes, it has great strength in its ability to describe the broad geometry of mountainous landscapes. In this way, the stream-power model is well-suited for our experiments. Because we focus on the range-scale slope, our results do not depend on either the dimensions of our model space or river channel topology. Furthermore, because we use normalized channel steepness as our measurement of fluvial relief, the exact values for *n* and *m* do not matter if the ratio between them is like that of expected landscapes (i.e., knowing the concavity is more important than knowing *n* or *m*). Earlier studies show that 0.46 is an appropriate concavity for rivers in the western Andes and northern Chile (*44*), and is in the middle of observed values from other natural landscapes (*34*). At the risk of over-interpreting our results or suggesting that *n* or *m* of a buried landscape could be estimated to a high degree of precision, we suggest that using values of *n* = 2 and *m* = 1, to yield a concavity of 0.5, is an accurate and conservative estimate for landscape modelling.

There is a well-described relationship between range-scale slope and fluvial relief within our dataset that is controlled primarily by river channel concavity. However, the expected relationship between any measurement of relief and rock uplift rate *U* or erodibility *K* will change as *n* is varied. For example, *n* = 1 predicts a liner relationship between channel steepness k_{sn} and *U*; in contrast, *n* = 2 describes a non-linear relationship such that increasing

U does not create proportional increases in k_{sn}. However, because K, n, and m are inter-related, Fig. 3 will hold as an accurate guide to considering the rock uplift rates in other landscapes outside of the Andes in landscapes where $m/n \approx 0.5$.

Assumption of uniform, steady-state paleo-landscapes

When compared to steady-state landscapes with uniform boundary conditions, non-steady or non-uniform landscapes will have different geometries. In a broad sense, this change in geometry can be defined by a change in concavity, where the concavity of the landscape is no longer directly related to the ratio of m and n but instead represents a change in channel steepness over space and time at constant m and n. Large-scale convexities (convex up) in both river channels and gross topographic profile can develop in landscapes that experience an increase in rock uplift rate, or where erodibility is higher in the upper reaches of the landscape (*47, 48*). Conversely, enhanced concavity in both river channel and gross topographic profile can develop in landscapes that experience a decrease in rock uplift rates over time or where higher erodibility values are found at lower elevations. Spatially non-uniform, but steady, rock uplift rates can also change the apparent concavity of a landscape, whereby landscapes become more concave when rock uplift rates increase toward the range crest and vice versa (*49*).

As pyroclastic density currents (PDCs) are fluidized flows that travel downslope, they often record large-scale topographic perturbations by changing the relative thickness of resulting ignimbrite deposits. For example, if a PDC erupted onto a landscape defined by steep vent-proximal reaches and gentler downslope portions, we might expect a similar change in the surface of ignimbrite deposit as well as a downslope thickening of the deposit, as observed for the c. 7700 ybp eruption of Mt Mazama (Crater Lake), OR (*50*). Similarly, the upper surface of an ignimbrite emplaced onto a relatively shallow slope that then entered a steeper portion of the landscape, will record this change in steepness. We emphasize our initial position that the important characteristic of an ignimbrite datum is an expansive surface that be roughly described by a surface slope, and that the deposit thins in a predictable manner away from the source. If these conditions hold, then any minor transient signals that may recorded in the paleo-topography are unlikely to reduce the accuracy of our solution.

Implications for rock uplift rates in the Central Andes

Our analysis suggests that the western flank of the Central Andes would have also experienced low rock uplift rates before the Miocene flare-up owing to the specifics of subduction zone convergence rates or fault geometries. The low-relief topographies that likely exist under the ignimbrites of the western Andes are similar to the lower elevation portions of the modern eastern Andean fold-and-thrust belt (*51*), the physiographic Lower Himalaya of central Nepal (*52*), and large portions of Taiwan (*53*). Despite having much higher rock uplift rates and erosion rates, Taiwan is thought to have much higher erodibility values, thus creating lower relief landscapes. Whereas the Lower Himalaya and portions of the Andean fold-and-thus belt have relatively low rock uplift rates due to the specifics of fault geometries.

Direct comparison of our results with those from thermochronology is difficult due to the different integration timescales. Most low-temperature thermochronometric cooling ages on the western Andean margin are Eocene, yielding low time-averaged rock uplift rates from ~50 Ma to the present of < 0.2 km Myr⁻¹ (*54*). By contrast, our estimate of rock uplift rate is integrated over the much shorter period of time required for the landscape to reach steady state. This is a function of the size of the range, the initial topography, as well as the erodibility and rock uplift rate. The length of our model domain and the initial river relief of 10 m yields a mountain range with a range-scale slope of 1.5° in ~14 Myr (at 95% steady-state), with $K = 4 \times 10^{-9}$ m⁻¹ yr⁻¹ and $U = 0.1$ km Myr⁻¹. Here the time to steady-state is inversely proportion to K. Fourteen million years is a rough estimate for how long steady rock uplift rates may have

been required to create a steady-state landscape, though steady rates could have persisted for longer. Even lower rock uplift/erosion rates have been suggested in the Late-Cretaceous and Palaeocene from low-temperature thermochronometry (*54*). These low rock uplift rates may be explained by low convergence rates from the Eocene to the early Miocene following the Incaic orogeny and before the Quechua orogeny (*55–58*). Indeed, exhumation rates that integrate over the Incaic orogeny are found to be greater than 0.25 km Myr^{-1} (*12*).

CONCULSIONS

Like other expansive and datable depositional or erosional surfaces, low aspect ratio ignimbrites are valuable data for constraining paleo-topographies and the boundary conditions that formed them. Because ignimbrites generally thin away from their source and form an upper surface described by a gentle slope, there is a limited suite of landscape geometries that can lie beneath them. These geometric constraints, coupled with a broad understanding of landscape erodibility, can be used to constrain tectonic histories. Importantly, ignimbrites that preserve a relatively low surface slope must cover relatively low relief landscapes. Low relief landscapes, in turn, are the result of either low rock uplift rates and commensurate low erosion rates, or high erodibility values due the prevalence of easily eroded bedrock or high precipitation rates.

Using the geometry of the Miocene flare-up ignimbrites in the western Andes and the theory of the stream-power model, we have been able to constrain Oligocene-Miocene rock uplift rates to at most 0.25 km Myr^{-1}, but more likely < 0.1 km Myr^{-1}. These results provide a powerful new independent constraint on the development of the western Andes during a period in their history that is difficult to constrain using conventional techniques such as low-temperature thermochronometry, but is in line with estimates of relatively slow subduction zone convergence.

We have used the Miocene flare-up in the western Andes as a case study in this paper, but the lessons learned are broadly applicable to other regions that preserve low aspect ratio ignimbrites. Specifically, the modelling results reported here provide a framework to constrain the paleo-topographies that may lie beneath other low aspect ratio ignimbrites, provided that there is good reason to suggest the river networks would have had concavity values close to 0.5. The transferability of our method could be improved with more precise values of *m* and/or *n*. Landscape modelling experiments could also improve our understanding of volcanic landscapes, particularly the relationship between eruption discharge, topographic roughness, and ignimbrite thickness or runout and improve estimates of ignimbrite volumes by predicting paleo-topographies and the rates and patterns of post-eruption erosion.
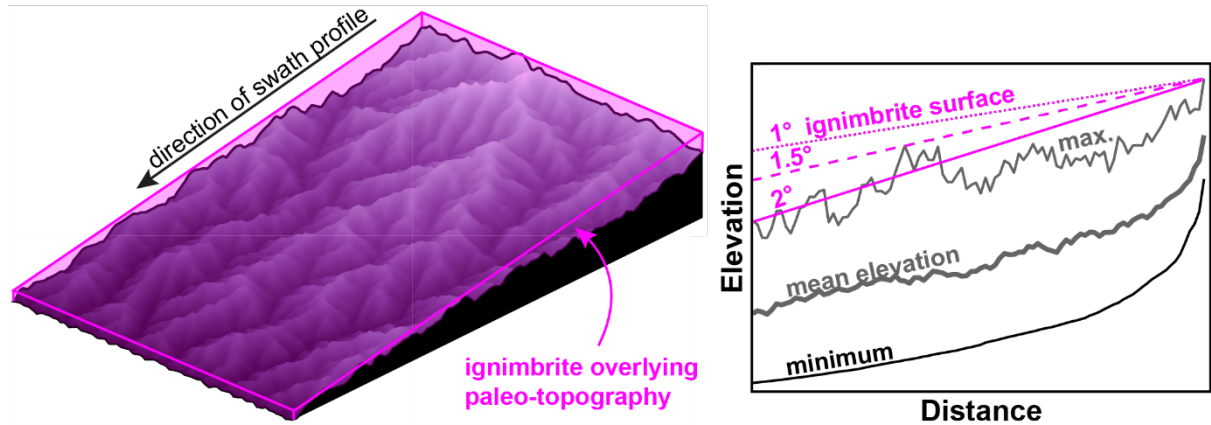
Figure 1. Burial of a mountainous landscape by a large-volume ignimbrite deposit. Note: the source of the ignimbrite is upslope of the displayed region in each panel. Left panel: oblique view of a synthetic landscape overlain by a deposit defined by a plane dipping parallel to the range-scale slope. Right panel: swath profile of the same synthetic landscape showing the minimum (thin black line), mean (thick grey line), maximum (thin grey line) elevations, and the surfaces of ignimbrite deposits with slopes of 1°, 1.5°, and 2° (magenta lines).
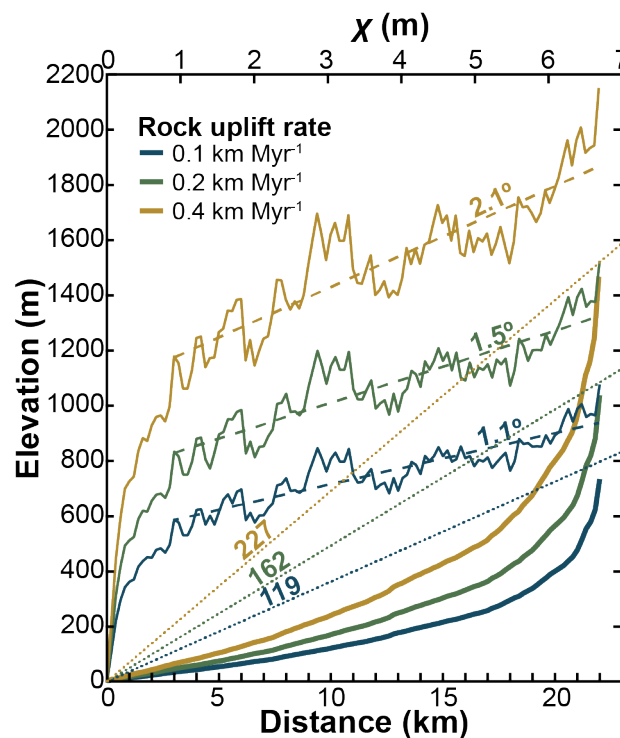

Figure 2. Swath profile data from three synthetic landscapes with the same erodibility ($K = 8$ x 10^{-9} m^{-1} yr^{-1}) and varying rock uplift rates. The minimum elevation (bold solid line), maximum elevation (thin solid line), regression of the maximum elevation (dashed lines, with slope values in degrees above), and a chi plot (dotted lines with channel steepness values above) are shown for each landscape. At these relatively low rock uplift rates there is a non-linear increase in the rang-scale slope, despite the linear increase in the rate.
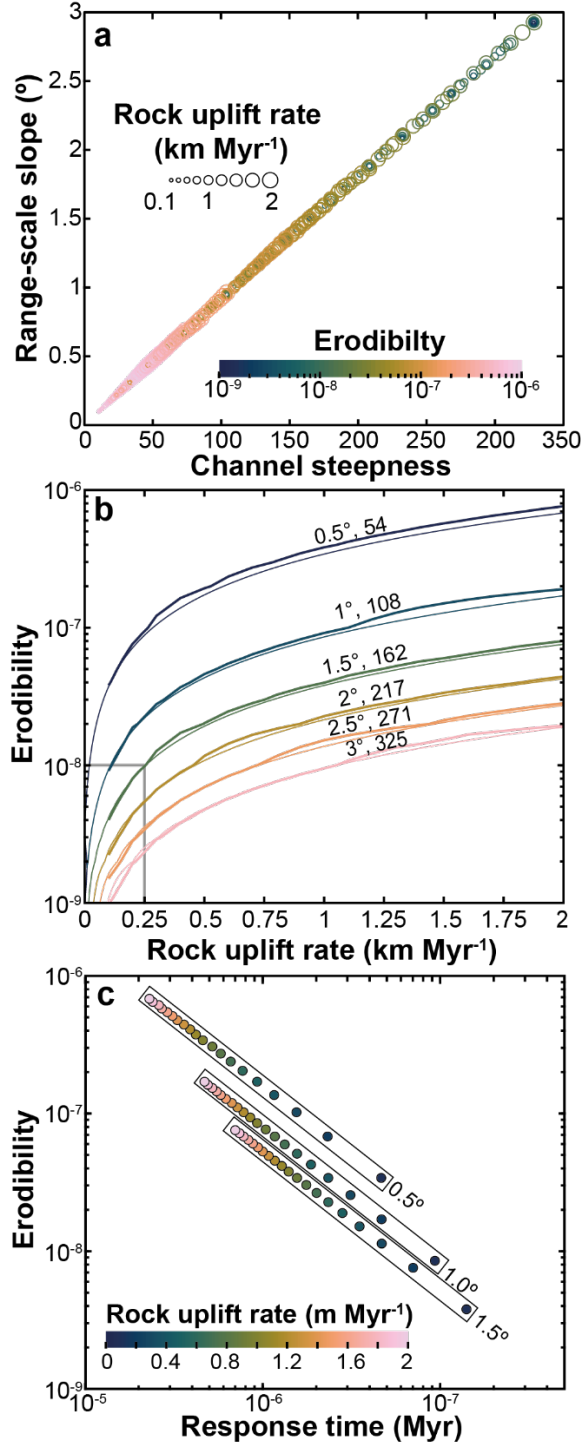
10

Figure 3. a) Comparison of channel steepness and range-scale slope (S_R) of maximum elevations from each model simulation. Data are colored by input erodibility values. Note that high erodibility values are restricted to low-relief landscapes. The slope of the relationship, k_{sn} = 108.3S_R, R^2 = 0.999, is set by the river concavity (e.g., equation 4 and 5). b) The variability of range-scale slope of maximum elevations from each combination of erodibility and rock uplift rate. Thick lines are contours through the landscape evolution model output and thin lines are analytical solutions from equation 6. The gray box denotes the plausible rock uplift rates for range-scale slopes less than 1.5° and erodibility values less than 1 x 10^{-8} m^{-1} yr^{-1}. c) Example of response times of landscapes to a new steady-state condition (calculated at 95% steady-state). Note that the response time is a function of the erodibility, rock uplift rate, and the final topographic state.

REFERENCES

1.   T. E. Jordan, B. L. Isacks, R. W. Allmendinger, J. A. Brewer, V. A. Ramos, C. J. Ando, Andean tectonics related to geometry of subducted Nazca plate. *GSA Bull.* **94**, 341–361 (1983).

2.   M. E. van Zalinge, R. S. J. Sparks, L. A. Evenstar, F. J. Cooper, J. Aslin, D. J. Condon, Using ignimbrites to quantify structural relief growth and understand deformation processes: Implications for the development of the Western Andean Slope, northernmost Chile. *Lithosphere*. **9**, 29–45 (2017).

3.   E. S. Platzman, R. S. J. Sparks, F. J. Cooper, Fabrics, facies, and flow through a large-volume ignimbrite: Pampa De Oxaya, Chile. *Bull. Volcanol.* **82**, 8 (2020).

4.   S. D. Willett, Orogeny and orography: The effects of erosion on the structure of mountain belts. *J. Geophys. Res.-Solid Earth*. **104**, 28957–28981 (1999).

5.   P. G. DeCelles, M. N. Ducea, P. Kapp, G. Zandt, Cyclicity in Cordilleran orogenic systems. *Nat. Geosci.* **2**, 251–257 (2009).

6.   C. N. Garzione, G. D. Hoke, J. C. Libarkin, S. Withers, B. MacFadden, J. Eiler, P. Ghosh, A. Mulch, Rise of the Andes. *Science*. **320**, 1304–1307 (2008).

7.   C. J. Poulsen, T. A. Ehlers, N. Insel, Onset of Convective Rainfall During Gradual Late Miocene Rise of the Central Andes. *Science*. **328**, 490–493 (2010).

8.   S. Lamb, P. Davis, Cenozoic climate change as a possible cause for the rise of the Andes. *Nature*. **425**, 792–797 (2003).

9.   K. M. Gregory-Wodzicki, Uplift history of the Central and Northern Andes: A review. *GSA Bull.* **112**, 1091–1105 (2000).

10.   P. W. Reiners, M. T. Brandon, Using Thermochronology to Understand Orogenic Erosion. *Annu. Rev. Earth Planet. Sci.* **34**, 419–466 (2006).

11.   E. J. F. Mutch, J. D. Blundy, B. C. Tattitch, F. J. Cooper, R. A. Brooker, An experimental study of amphibole stability in low-pressure granitic magmas and a revised Al-in-hornblende geobarometer. *Contrib. Mineral. Petrol.* **171**, 85 (2016).

12.   S. I. R. Dahlström, F. J. Cooper, J. Blundy, S. Tapster, J. Cortés Yáñez, L. A. Evenstar, Pluton Exhumation in the Precordillera of Northern Chile (17.8°–24.2°S): Implications for the Formation, Enrichment, and Preservation of Porphyry Copper Deposits. *Econ. Geol.* (2022), doi:10.5382/econgeo.4912.

13.   L. Goren, M. Fox, S. D. Willett, Tectonics from fluvial topography using formal linear inversion: Theory and applications to the Inyo Mountains, California. *J. Geophys. Res. Earth Surf.* **119**, 1651–1681 (2014).

14.   B. A. Adams, K. X. Whipple, A. M. Forte, A. M. Heimsath, K. V. Hodges, Climate controls on erosion in tectonically active landscapes. *Sci. Adv.* **6**, eaaz3166 (2020).

15.   K. X. Whipple, G. E. Tucker, Dynamics of the stream-power river incision model: Implications for height limits of mountain ranges, landscape response timescales, and research needs. *J. Geophys. Res.-Solid Earth*. **104**, 17661–17674 (1999).

16.   M. García, M. Gardeweg, J. Clavero, G. Hérail, Arica map: Tarapacá Region, scale 1: 250,000. *Carta Geológica Chile Ser. Geol. Básica*. **84** (2004).

17.   G. Wörner, K. Hammerschmidt, F. Henjes-Kunst, J. Lezaun, H. Wilke, Geochronology (40Ar/39Ar, K-Ar and He-exposure ages) of Cenozoic magmatic rocks from Northern Chile (18-22°S): implications for magmatism and tectonic evolution of the central Andes. *Rev. Geológica Chile*. **27**, 205–240 (2000).

18.   G. P. L. Walker, Grain-Size Characteristics of Pyroclastic Deposits. *J. Geol.* **79**, 696–714 (1971).

19.   R. A. F. Cas, J. V. Wright, in *Volcanic Successions Modern and Ancient* (Springer Netherlands, Dordrecht, 1988; http://link.springer.com/10.1007/978-94-009-3167-1_8), pp. 222–266.

20.   R. S. J. Sparks, L. Wilson, A model for the formation of ignimbrite by gravitational column collapse. *J. Geol. Soc.* **132**, 441–451 (1976).

21.   S. D. Silva, G. Zandt, R. Trumbull, J. G. Viramonte, G. Salas, N. Jiménez, Large ignimbrite eruptions and volcano-tectonic depressions in the Central Andes: a thermomechanical perspective. *Geol. Soc. Lond. Spec. Publ.* **269**, 47–63 (2006).

22.   G. P. L. Walker, Ignimbrite types and ignimbrite problems. *J. Volcanol. Geotherm. Res.* **17**, 65–88 (1983).

23.   C. Wilson, Ignimbrite morphology and the effects of erosion: a New Zealand case study. *Bull. Volcanol.* **53**, 635–644 (1991).

24.   K. X. Whipple, Bedrock rivers and the geomorphology of active orogens. *Annu. Rev. Earth Planet. Sci.* **32**, 151–185 (2004).

25.   A. D. Howard, G. Kerby, Channel changes in badlands. *Geol. Soc. Am. Bull.* **94**, 739–752 (1983).

26.   J. Flint, Stream gradient as a function of order, magnitude, and discharge. *Water Resour. Res.* **10**, 969–973 (1974).

27.   J. T. Hack, "Studies of longitudinal stream profiles in Virginia and Maryland," *Shorter Contributions to General Geology* (United State Department of the Interior, 1957), pp. 41–97.

28.   J. D. Stock, D. R. Montgomery, Geologic constraints on bedrock river incision using the stream power law. *J. Geophys. Res. Solid Earth 1978–2012*. **104**, 4983–4993 (1999).

29.   K. X. Whipple, N. P. Snyder, K. Dollenmayer, Rates and processes of bedrock incision by the Upper Ukak River since the 1912 Novarupta ash flow in the Valley of Ten Thousand Smokes, Alaska. *Geology*. **28**, 835–838 (2000).

30.   P. van der Beek, P. Bishop, Cenozoic river profile development in the Upper Lachlan catchment (SE Australia) as a test of quantitative fluvial incision models. *J. Geophys. Res. Solid Earth*. **108**, JB002125 (2003).

31.   B. Campforts, V. Vanacker, F. Herman, M. Vanmaercke, W. Schwanghart, G. E. Tenorio, P. Willems, G. Govers, Parameterization of river incision models requires accounting for environmental heterogeneity: insights from the tropical Andes. *Earth Surf. Dyn.* **8**, 447–470 (2020).

32.   J. R. Zondervan, A. C. Whittaker, R. E. Bell, S. E. Watkins, S. A. S. Brooke, M. G. Hann, New constraints on bedrock erodibility and landscape response times upstream of an active fault. *Geomorphology*. **351**, 106937 (2020).

33.   K. L. Ferrier, K. L. Huppert, J. T. Perron, Climatic control of bedrock river incision. *Nature*. **496**, 206–209 (2013).

34.   C. Wobus, K. X. Whipple, E. Kirby, N. Snyder, J. Johnson, K. Spyropolou, B. Crosby, D. Sheehan, Tectonics from topography: Procedures, promise, and pitfalls. *Geol. Soc. Am. Spec. Pap.* **398**, 55–74 (2006).

35.   W. B. Ouimet, K. X. Whipple, D. E. Granger, Beyond threshold hillslopes: Channel adjustment to base-level fall in tectonically active mountain ranges. *Geology*. **37**, 579–582 (2009).

36.   R. A. DiBiase, K. X. Whipple, A. M. Heimsath, W. B. Ouimet, Landscape form and millennial erosion rates in the San Gabriel Mountains, CA. *Earth Planet. Sci. Lett.* **289**, 134–144 (2010).

37.	D. Lague, The stream power river incision model: evidence, theory and beyond. *Earth Surf. Process. Landf.* **39**, 38–61 (2014).

38.	M.-A. Harel, S. M. Mudd, M. Attal, Global analysis of the stream power law parameters based on worldwide 10 Be denudation rates. *Geomorphology*. **268**, 184–196 (2016).

39.	D. E. J. Hobley, J. M. Adams, S. S. Nudurupati, E. W. H. Hutton, N. M. Gasparini, E. Istanbulluoglu, G. E. Tucker, Creative computing with Landlab: an open-source toolkit for building, coupling, and exploring two-dimensional numerical models of Earth-surface dynamics. *Earth Surf. Dyn.* **5**, 21–46 (2017).

40.	J. S. Leonard, K. X. Whipple, *J. Geophys. Res. Earth Surf.*, in press, doi:10.1029/2021JF006183.

41.	K. R. Barnhart, G. E. Tucker, S. G. Doty, C. M. Shobe, R. C. Glade, M. W. Rossi, M. C. Hill, *J. Geophys. Res. Earth Surf.*, in press, doi:10.1029/2019JF005287.

42.	T. E. Jordan, N. E. Kirk-Lawlor, N. P. Blanco, J. A. Rech, N. J. Cosentino, Landscape modification in response to repeated onset of hyperarid paleoclimate states since 14 Ma, Atacama Desert, Chile. *GSA Bull.* **126**, 1016–1046 (2014).

43.	J. M. Shaw, L. Evenstar, F. J. Cooper, B. A. Adams, A. J. Boyce, F. Hofmann, K. A. Farley, *Geochem. Geophys. Geosystems*, in press, doi:10.1029/2021GC009759.

44.	F. Cooper, B. Adams, J. Blundy, K. Farley, R. McKeon, A. Ruggiero, Aridity-induced Miocene canyon incision in the Central Andes. *Geology*. **44**, 675–678 (2016).

45.	M. Fox, T. Bodin, D. L. Shuster, Abrupt changes in the rate of Andean Plateau uplift from reversible jump Markov Chain Monte Carlo inversion of river profiles. *Geomorphology*. **238**, 1–14 (2015).

46.	K. X. Whipple, B. J. Meade, Orogen response to changes in climatic and tectonic forcing. *Earth Planet. Sci. Lett.* **243**, 218–228 (2006).

47.	S. Bonnet, A. Crave, Landscape response to climate change: Insights from experimental modeling and implications for tectonic versus climatic uplift of topography. *Geology*. **31**, 123–126 (2003).

48.	B. A. Adams, K. V. Hodges, K. X. Whipple, T. A. Ehlers, M. C. van Soest, J.-A. Wartho, Constraints on the tectonic and landscape evolution of the Bhutan Himalaya from thermochronometry. *Tectonics*. **34**, 1329–1347 (2015).

49.	H. W. Beeson, S. W. McCoy, Geomorphic signatures of the transient fluvial response to tilting. *Earth Surf. Dyn.* **8**, 123–159 (2020).

50.	T. H. Druitt, C. R. Bacon, Lithic breccia and ignimbrite erupted during the collapse of Crater Lake Caldera, Oregon. *J. Volcanol. Geotherm. Res.* **29**, 1–32 (1986).

51.	N. M. Gasparini, K. X. Whipple, Diagnosing climatic and tectonic controls on topography: Eastern flank of the northern Bolivian Andes. *Lithosphere*. **6**, 230–250 (2014).

52.	C. Wobus, A. Heimsath, K. Whipple, K. Hodges, Active out-of-sequence thrust faulting in the central Nepalese Himalaya. *Nature*. **434**, 1008–1011 (2005).

53.	M. G. Fellin, C.-Y. Chen, S. D. Willett, M. Christl, Y.-G. Chen, Erosion rates across space and timescales from a multi-proxy study of rivers of eastern Taiwan. *Glob. Planet. Change*. **157**, 174–193 (2017).

54.	N. N. Avdievitch, T. A. Ehlers, C. Glotzbach, Slow Long-Term Exhumation of the West Central Andean Plate Boundary, Chile. *Tectonics*. **37**, 2243–2267 (2018).

55.	M. Sdrolias, R. D. Müller, Controls on back-arc basin formation. *Geochem. Geophys. Geosystems*. **7**, GC001090 (2006).

56.   P. Soler, M. G. Bonhomme, in *Geological Society of America Special Papers* (Geological Society of America, 1990; https://pubs.geoscienceworld.org/books/book/379/chapter/3797132/), vol. 241, pp. 173–192.

57.   R. Somoza, Updated azca (Farallon)—South America relative motions during the last 40 My: implications for mountain building in the central Andean region. *J. South Am. Earth Sci.* **11**, 211–215 (1998).

58.   F. Pardo-Casas, P. Molnar, Relative motion of the Nazca (Farallon) and South American Plates since Late Cretaceous time. *Tectonics*. **6**, 233–248 (1987).